Anisotropy of water dynamics confined in model silica material

Hassan Khoder, Jean-Marc Zanotti, Jacques Ollivier, Xavier Le Goff, Renaud Podor, Diane Rébiscoul

Anisotropy of water dynamics confined in model silica material

Hassan KHODER[*†], *Jean-Marc ZANOTTI*[‡], *Jacques OLLIVIER*[§], *Xavier LE Goff*[†], *Renaud PODOR*[†], *Diane REBISCOUL*[*†]

[†] Univ Montpellier, CEA, CNRS, ENSCM, ICSM, 30207 Bagnols-sur-Cèze Cedex, France

[‡] Laboratoire Léon Brillouin, UMR CEA-CNRS 12, CEA Saclay, 91191 Gif-sur-Yvette, France

[§] Institut Laue-Langevin, 6 rue J. Horowitz, BP 156, F-38042 Grenoble, France

[*] Corresponding authors: hassan.khoder@hotmail.com diane.rebiscoul@cea.fr

Abstract

Silica microfibers with highly oriented cylindrical mesopores embedded in alumina membrane were used as model system to characterize the water dynamics anisotropy at a picosecond timescale. To reach this goal, we first studied the optimal preparation conditions to obtain longitudinal silica mesopores orientation at macroscopic scale. Accordingly, we characterized the impact of ethanol content and aspiration pressure on the orientation and filling of the mesopores using scanning electron microscopy, transmission electron microscopy, small angle X-ray scattering, and dynamic vapor sorption. Based on the obtained results we selected the most appropriate sample as a model system. The model system was filled with water and used to characterize the dynamics of water molecules in parallel and perpendicular directions using quasi-elastic neutron scattering measurements collected in two orientations at two timescales (7 ps and 30 ps). The results revealed the anisotropy of water dynamics in the silica mesopores and highlighted a larger perpendicular diffusion coefficient compared to the parallel one at both timescales. This suggests that it may be more difficult for water molecules to move from one hydroxyl surface site to another compared to forming a hydrogen bond with a water molecule not adsorbed at the surface.

Keywords:

Nanoconfined water

Water dynamics anisotropy

Mesopores orientation

Quasi-Elastic Neutron Scattering

1. Introduction

The properties of water confined in a limited volume of few nanometers are modified compared to bulk water. This change in properties is due to the interaction between a high fraction of water and the solid surface. These changes affect many physical and chemical processes at the origin of the macroscopic behavior of nanoporous materials in aqueous solution, such as solution transport [1], ion adsorption [2], dissolution [3,4], phase precipitation [5–9], chemical reactivity [10], *etc*. The determination of these modifications is of interest for predicting the evolution of these materials in solution, such as the case for cement, membranes, rocks, minerals, catalytic materials, and various other materials present in the geological repository of nuclear wastes such as geopolymers, corrosion products, clay, and glass alteration layers. Indeed, the prediction of their long-term behavior can have a direct impact on the sizing of the industrial system.

Water dynamics is one of the essential properties affecting physical and chemical processes occurring in nanoconfinement. Water dynamics at the picosecond timescale, as characterized by quasi-elastic neutron scattering, has been recently identified as one of the main factors driving the chemical reactions occurring in confined media filled with water and ions [4,11]. Since industrial or natural materials consist of a set of nanopores having various sizes and orientations and high tortuosity, water dynamics is generally characterized within highly controlled nanopores from MCM-41 [12] and SBA-15 [13] mesoporous silica synthesized by self-assembling mechanism using surfactant molecules. The use of these materials has led to several key findings about water motions at various timescales. Indeed, it has been shown that water dynamics depends on the pore filling [14,15], the pore size [16–19], the density of ions adsorbed at the pore surface [19], and the properties of the pore surface such as the roughness [20] and its chemical composition [11,18,21]. However, the use of these materials gives access to a set of isotropic water motions due to the presence of a mixture of coherent

domains of oriented nanopores with a size of a few hundred nanometers. This type of confining system does not allow the investigation of the anisotropy of water transport from the molecular to the macroscopic scale in a continuous way. For this purpose, materials with homogenous nanopores oriented and continuous on macroscopic scale must be used.

Silica microfibers with highly oriented cylindrical mesopores embedded in alumina membrane is an interesting model system to reach this goal. Its preparation was already studied by Yamaguchi et al. [22], and others [23–26]. This method is based on the aspiration of a silica precursor solution containing a templating agent onto an anodic alumina membrane having vertically aligned pores. The alumina vertically aligned pores, the amount of solvent and the aspiration inducing solvent evaporation drive the formation of 1D mesostructured mesoporosity released after thermal treatment.

In this study, these silica microfibers with highly oriented cylindrical mesopores embedded in alumina membrane were used as silica model system to characterize the water dynamics anisotropy at a picosecond timescale. To reach this goal, we first studied the optimal preparation conditions to obtain longitudinal silica mesopores orientation at macroscopic scale. Using scanning electron microscopy, transmission electron microscopy, small angles X-ray scattering, and dynamic vapor sorption, we precisely characterized the impact of the ethanol content and the aspiration pressure on the orientation and the length of the silica mesopores. These results allowed the selection of the most appropriate sample as a model system. This model system filled with water was used to characterize the dynamics of water molecules in parallel and perpendicular directions using quasi-elastic neutron scattering measurements collected in two orientations at two timescales 7 ps and 30 ps.

2. Materials and methods

2.1. Preparation of hybrid alumina membrane

To synthesize highly oriented mesoporous silica microfibers within the alumina membrane, a silica precursor solution (sol) was introduced into the large pores of anodic alumina membranes (WHA68096002) by aspiration as illustrated in Fig. 1. The alumina membranes used in this work present a non-uniform pore diameter varying from 30 nm on the front side to 200 nm on the backside (see Fig. A.1).

The sols were prepared as follows [27]. First, 1.0 g of surfactant Pluronic P123 ($EO_{20}PO_{70}EO_{20}$; EO = ethylene oxide, PO = propylene oxide) was dissolved in mixtures of 4, 8, 15, 20, or 25 g of ethanol, 0.1 g of concentrated HCl solution at 12 M, and 2.0 g of H_2O. The solutions were stirred for 1 h under reflux. Second, 2.13 g of TEOS were added dropwise to the mixtures and then stirred at 60 °C for 12 h to obtain the sols. Third, 2 to 7 ml of sol were dropped onto the alumina membrane placed in a filtration setup connected to a vacuum system at a pressure varying between 10 and 50 kPa. Finally, the filled membranes were dried under aspiration for 5 min at room temperature and calcined at 500 °C for 5 h (4 °C/min) to remove the surfactant.

Table 1 presents the sample references regarding the amount of ethanol in the sol and the aspiration pressure used to fill the alumina pores. Hereafter, the prepared membranes will be referred to: ‘xEt_y’, where x is the mass (g) of ethanol added to the sol and y is the aspiration pressure (kPa).

2.2. Solid Characterizations

2.2.1. Scanning Electron Microscopy (SEM)

The synthesized hybrid membranes were characterized by SEM to estimate the silica filling ratio inside the alumina pores. The SEM used is a QUANTA 200 ESEM FEG (FEI, Eindhoven, Netherlands). Moreover, inside the SEM chamber, we applied an acceleration

voltage of 4.2 KV, while the water pressure was maintained at 10 Pa to limit the charge accumulation on the surface of the sample. The images shown in this paper were obtained with a Circular Backscatter Detector provided by the FEI company, which employs the back scattered electron mode [28].

2.2.2. Transmission Electron Microscopy (TEM)

TEM was performed on a JEOL JEM-1400F operated with an accelerating voltage of 100 kV to observe the morphology of the silica mesopores. To reach this goal, the alumina part of the samples was dissolved in 10 wt% phosphoric acid (H_3PO_4) for 24 h. Thereafter, the sample suspension was deposited on the holey grids.

2.2.3. Small Angle X-ray Scattering (SAXS)

SAXS analyses were performed to study the porous silica mesostructure of the different samples. The SAXS data were collected in transmission geometry using Xenocs setup with a molybdenum anode delivering a wavelength of 0.71 Å. This short wavelength allows the coverage of a scattering vector, q, ranging from 0.2 nm^{-1} to 20 nm^{-1}. The collimation was ensured by a Fox2D multilayer mirror and a set of scatterless slits that delimitated the beam to a square section (0.8 mm side length at the sample position). The distance from the sample to the detector was about 750 mm and was calibrated using silver behenate powder. SAXS patterns were recorded on a MAR345 imaging plate detector, and azimuthal averaging of 2D data was performed using the FIT2D software. The scattered intensity was calculated in the absolute scale (cm^{-1}) and expressed as a function of the magnitude of the scattering vector $q = (4\pi\sin\theta)/\lambda$, where θ is the scattering angle. Four membranes prepared in the same experimental conditions were used for each analysis to increase the scattered intensity.

2.2.4. Dynamic Vapor Sorption (DVS)

Water adsorption-desorption isotherms of the hybrid alumina membranes were measured with DVS to determine the porous texture characteristics. Samples were outgassed before

analysis at 200 °C for 24 h. DVS allows measuring the change in mass while varying the relative humidity surrounding the sample located in a pan suspended on an ultra-sensitive microbalance. Then, a complete cycle of adsorption/desorption is measured with a stepwise of P/P_0 = 10 %. The equilibrium state is defined manually considering a change in mass ≤ 0.001 %/min during 10 minutes.

2.2.5. Quasi-Elastic Neutron Scattering (QENS)

The picosecond scale water dynamics was studied at 20°C by QENS on the IN5 time-of-flight spectrometer (Institut Laue-Langevin, Grenoble) [29], with 2 incident wavelengths of 4.8 and 8 Å, corresponding to elastic energy resolutions of 86 and 22 μeV respectively (data availability [30]). These experimental conditions allow timescale observations of about 7 ps and 30 ps. The scattered intensity was collected for two sample orientations, 45° and 135°, to obtain the dynamics of water in both parallel and perpendicular orientations, respectively. First, the instrumental resolution was determined using the incoherent elastic scattering of a vanadium foil. Second, 10 hybrid alumina membranes dried at 200°C during 4 days in an oven under vacuum and 10 water filled hybrid alumina membranes were analyzed in order to have sufficient signal intensity. For their water filling, the hybrid alumina membranes were placed in a desiccator in the presence of a beaker containing a saturated solution of KCl, fixing a relative humidity (RH) of 83 % at 25 °C. At this humidity, water only fills the mesopores [18]. Samples were stored in this condition for 10 days and then placed into aluminum cells sealed with an indium wire to avoid water loss and ensure a constant hydration level during neutron scattering experiments. Thereafter, data analysis was performed between -2 and 2 meV at Q = 1.85 $Å^{-1}$ for λ=4.8 Å and between -0.5 and 0.5 meV at Q = 1.11 $Å^{-1}$ for λ=8 Å. These data were treated using the QENSH program provided by LLB dedicated to this kind of treatment [31].

3. Results and discussion

3.1. Preparation and selection of the model system

To select the most adapted model system, the impact of ethanol amount in the sol and the aspiration pressure used to prepare the samples were characterized.

3.1.1. Quantification of the filling of alumina pores

The filling ratios R of the pores of the hybrid alumina membranes were determined from the SEM images of the filled membrane surfaces (Fig. 2). These images were analyzed with ImageJ software [32] to determine the filling degree of silica in each membrane as described in Appendix B (silica is shown in grey inside the pores in Fig. 2).

The obtained results presented in Table 2 show that for a specific ethanol content in the sol, the filling ratio strongly depends on the aspiration pressure. The highest R was obtained for the samples 4Et_50 and 15Et_20.

In addition, silica mass density per volume of alumina, d_{SiO_2}, was estimated from R and the average length of the silica microfibers, which was determined from TEM images of silica microfibers (Fig. A.2). The results show that the average length of the silica microfibers is comprised between 8 and 11 μm, which is consistent with the results obtained by Meoto et al. [26] and Yamaguchi et al. [22] Thereafter, only the samples presenting the highest ratio R for each ethanol amount were analyzed.

3.1.2. Determination of the silica microfibers mesostructure

To determine the porous silica mesostructure, selected samples were analyzed by SAXS, and the results are presented in Fig. 3 (a) in absolute scattered intensity. The absolute intensity calculation method is presented in appendix B.

As presented in Fig. 3 (a), two Bragg reflection peaks (B1 (10) and B2 (11)) characteristics of a hexagonal lattice of the pores [33] can be observed. These peaks present various intensities, widths, and positions that can be explained by the pore size distributions and the

paracrystalline disorders on the 2D lattice. As illustrated in Table 3, the increase in the ethanol loading leads to a decrease in the spacing $d_{10} = \frac{2\pi}{q_{10}}$ and the unit cell parameter $a = \frac{2d_{10}}{\sqrt{3}}$ indicating a decrease in the pore size and/or the wall thickness. In addition, the intensity of the peak B1 goes with the silica mass density in the membranes (Fig. 3 (b)).

3.1.3. Determination of the mesopores orientation

The mesopores orientation of the silica microfibers was analyzed by TEM after complete etching of the alumina part with a 10 wt% phosphoric acid (H_3PO_4) for 24 h. The TEM images of the different samples are presented in Fig. 4.

Fig. 4 shows the samples having fiber morphology. The results reveal the existence of three types of porous silica mesostructures depending on the ethanol content and the aspiration pressure. The samples 15Et_20 and 20Et_15 present a 1D mesopores orientation aligned along the microfibers. This orientation is reproducible for all the microfibers analyzed by TEM as displayed in Fig. A.3. This anisotropy was not detected by SAXS probably due to the use of four membranes stacked on top of each other for the analysis. Decreasing the ethanol content to from 15 to 8 and 4 g in the sol, two types of mesopores orientations can be observed depending on the aspiration pressure. For the samples, 8Et_40 and 4Et_20, an arrangement of a 3D domain of hexagonal mesopores is obtained. This network is characterized by an inter-pore distance of 10.5 nm measured from the unit cell parameter calculated from the SAXS patterns (Table 3) and confirmed by TEM images (Fig. A.4). For the samples, 8Et_20 and 4Et_50, a 1D:3D mixture of mesopores orientation is obtained. Based on these results, the 1D mesopores orientation is favored at high ethanol loading and low aspiration pressure (15Et_20 and 20Et_15 samples).

3.1.4. Porous textural properties

To determine the porous texture characteristics of the selected samples, water adsorption-desorption isotherms were measured with DVS and are shown in Fig. 5 (a). Specific surface areas, pore volumes, and pore size distributions were obtained using the Brunauer-Emmett-Teller (BET) method and the Barret−Joyner−Halenda (BJH) model. The obtained results are presented in Table 3.

These results show that increasing the ethanol loading in the sol leads to a decrease in the mass of adsorbed water within the samples and then the calculated S_{BET} and V_p. Thus, it is only possible to determine a pore size range for samples presenting sufficient water filling. This is the case for the samples synthesized with 4, 8 and 15 g of ethanol. Regarding the number of experimental measurements in Fig. 5 (b), the mean pore diameter can be estimated to be 5.5 ± 1 nm. In addition, the increase of the signal intensity for pores smaller than 2 nm, is due to the presence of micropores resulting from the P123 surfactant templating as classically observed in SBA-15 silica material. This microporosity generally consists of 10% of the total porous volume [34]. As revealed by the TEM analysis presented previously in Fig. 4, the length of the mesopores may play a role. Indeed, as illustrated in Fig. 5 (c), the samples 4Et_50 and 15Et_20 present continuous water adsorption when they are exposed to RH = 95%. However, the adsorption rate of water vapor through the mesopores of the sample 15Et_20 is significantly slower. Indeed, the 3D mesopores orientation in the sample 4Et_50 leads to a shorter pore length resulting in a rapid filling rate of water vapor diffusion. This finding is supported by other studies showing that increasing the pore length decreases the adsorption rate [35,36]. These results highlight the need for a long exposure to reach the real equilibrium and the complete filling of the 1D mesopores.

3.1.5. Choice of the model system

The results presented so far show the impact of the ethanol content and the aspiration pressure on the silica filling degree and the mesopores orientation. Three factors may affect the alumina pores filling. The first one is the viscosity of the sol that pilots its penetration into the pores. The second one is the silica precursor concentration in the sol that drives the silica condensation rate and thus, the formation of a sufficient rigid silica network when the mesophase is formed. The last one is the surfactant concentration in the sol that drives the formation of the mesophase during the alumina pores filling. This deposition process can be compared to the mechanism of "Evaporation-Induced Self-Assembly (EISA)" occurring during mesophase thin layer deposition [37,38]. Here, the highest filling degree of silica having a 1D mesopores orientation was obtained for hybrid alumina membranes prepared with a sol of 15 to 20 g of ethanol and dropped with an aspiration pressure of 15 to 20 kPa. Therefore, the 15Et_20 sample was selected as a model system to study the water dynamics anisotropy.

3.2. Water dynamics at picosecond timescale

The dynamics of water molecules confined in the sample 15Et_20 at the picosecond scale was studied. QENS spectra were collected for 10 dried and 10 same water filled samples. The scattered intensity was collected for two sample orientations, 45° and 135°, to obtain the dynamics of water molecules in both parallel and perpendicular orientations respectively, as described on Fig. 6 (a).

Fig. 7 (a) and (b) show the QENS spectra collected at λ = 4.8 and 8 Å respectively. These spectra include several contributions: the sample cell, the alumina membrane, the silica, the hydroxyl groups of the pore surface, and the confined water. Empty membrane measured in a dried state (200 °C for 4 days) involves the four first contributions. Since the incoherent scattering cross-section of hydrogen is large, the main contribution to the scattering intensity comes from hydrogen. Consequently, the spectra reflect the probability of neutrons to be

scattered by the protons of the sample. The signal broadening observed for the samples when compared to the elastic resolution-broadened scattering of the vanadium is related to the energy transfer between incoming neutrons and the diffusing protons belonging to water molecules. The broadening observed for the dry membrane suggests the presence of residual water at the silica pore surface after the drying process.

Fig. 7 (a) and (b) show a broadening in the quasi-elastic when comparing the hydrated and dry samples. The associated relaxations are characteristic of the water motions. This broadening is more pronounced for the perpendicular sample orientation, highlighting a water dynamics anisotropy. To demonstrate this point, we have first fitted the data of the Fig. 7 (a) with the model of Texeira et al [39] that expresses the dynamic structure factor S(Q,ω) using one elastic and two Lorentzian functions.

$$S(Q,\omega) = \exp\left(-(Q^2\langle u^2\rangle)/3\right)[C\delta(\omega)+(1-C)\, S_T(Q,\omega)\otimes S_{rot}(Q,\omega)]+B(Q) \qquad (1)$$

where Q and ω represent momentum and energy transfers, respectively. $\langle u^2\rangle$ is the mean-square vibrational amplitude. δ(ω) is a δ-function and corresponds to the elastic component. $(1-C)S_T(Q,\omega)\otimes S_{rot}(Q,\omega)$ represents the quasi-elastic component. C is the fraction of the elastic component. ⊗ indicates a convolution between $S_T(Q,\omega)$ and $S_{rot}(Q,\omega)$, which correspond to the contributions from translational and rotational diffusions of the confined water molecules, respectively.

The parameters obtained from the fitting of the parallel spectra were used and fixed to fit the perpendicular one. As it shown in Fig. 8 (a) and (b), it is not possible to fit both orientations with the same fitting parameters. This highlights an anisotropy of the water dynamics. Thus, it is necessary to use an appropriate model that predicts the intensity distribution of scattered neutrons and can accurately describe the anisotropy of water dynamics in our samples.

Consequently, we used the model of Dianoux et al. [40] which has been recently applied to clay materials [41]. To use this model, a diffusion equation for the water molecular motions has first to be solved to calculate the Van Hove self-correlation function $G_S(r, t)$ [42]. The incoherent scattering function $S_{inc}(Q, \omega)$ is then obtained by double Fourier transform of $G_S(r, t)$ with respect to both, space and time. The intensity distribution of scattered neutrons can finally be predicted from $S_{inc}(Q, \omega)$ as a function of the energy and the momentum transferred in the scattering process.

In the case of water transport considered in this study, it is reasonable to assume a Fick–like diffusion neglecting rotations and more complex relaxations such as coupled translation-rotations or jump-like diffusions, which dominate only at large Q-values outside of the Q-window of interest in these measurements. Vineyard [43] showed that the mathematical solution of the diffusion equation, $G_S(r,t)$, can be written as eq 2.

$$G_S(r,t) = (4\pi Dt)^{-3/2}\exp(-r^2/4Dt) \qquad (2)$$

Its Fourier transform gives the incoherent scattering function $S_{inc}(Q,\omega)$ (eq 3).

$$S_{inc}(Q,\omega) = (1/\pi)\,(DQ^2/((DQ^2)^2+\omega^2)) \qquad (3)$$

Equation 3 is a Lorentzian function having a full width at half maximum (FWHM) of $2DQ^2$. The translational part of the scattering signal can be fitted using a modified version of this equation applied for systems with axial anisotropy following the eq 4 [40,41].

$$S_{inc}(Q, \omega) = (1/\pi)\,((D_{//}\cos^2\beta + D_{\perp}\sin^2\beta)Q^2)/((D_{//}\cos^2\beta + D_{\perp}\sin^2\beta)^2\, Q^4+\omega^2) \qquad (4)$$

With $D_{//}$ and $D_{\perp}$ are the diffusion coefficients along and perpendicular to the pore axis respectively (Fig. 6 (b)), and β is the angle between Q and the pore axis (0° for parallel orientation and 90° for perpendicular orientation). This model was used to fit the experimental

scattered intensities at different Q values. The obtained results corresponding to Q = 1.85 $Å^{-1}$ and λ = 4.8 Å are presented on Fig. 9 (a) and (b) and the ones obtained for Q = 1.11 $Å^{-1}$ and λ = 8 Å are presented on Fig. 9 (c) and (d).

The parallel and perpendicular diffusion coefficients obtained from the fitting of the spectra at the parallel and perpendicular Q values respectively were used and fixed to fit the different Q values. The obtained results are shown in Fig. D.1 and Fig. D.2 for λ = 4.8 Å and in Fig. D.3 and Fig. D.4 for λ = 8 Å. It can be observed that the model perfectly fits the data at all Q values. The obtained results, presented in Table 4, reveal the anisotropy of water dynamics in the silica mesopores and highlight a higher perpendicular diffusion coefficient, $D_{\perp}$ compared to the parallel one, $D_{//}$.

These values also show first a global slow-down of the water dynamics due to confinement. Indeed, the diffusion coefficients obtained in this study are lower than that of bulk water, which is generally close to $2.2 \pm 0.1 \times 10^{-9}$ m^2 s^{-1} [19,39]. Moreover, the diffusion coefficients obtained at λ = 4.8 Å in this study are close to the one obtained in [19] at λ = 4.32 Å in SBA-15 silica having pore size close to our sample. Notably, the water dynamics depend on the analyzed timescale, as evidenced by the fact that the diffusion coefficients at λ = 8 Å are 3 to 4 times lower than those at λ = 4.8 Å. This has already been observed with water confined in MCM-41 and others nanoporous hybrid materials [21] analyzed at two different wavelengths. It may be associated with the existence of non-mobile water not probed at a shorter timescale. Indeed, in silica mesopores a fraction of water molecules strongly interacts with the hydroxyl groups of the silica surface slowing down their dynamics. Several experimental and modeling studies have confirmed these observations [11,14,18,19,44–50]. However, in the quoted studies, the difference in diffusion coefficients at two wavelengths is generally not as high as for our samples. This may be partially explained by the additional contribution of the water molecules in the pore wall microporosity which contributes to 10% of the overall porosity

(Fig. 5 (b)). Indeed, in pores smaller than 2 nm, water molecules are strongly slowed down, which may also explain the slight decrease of Para/Perp ratio from 0.68 at 7 ps to 0.57 at 30 ps. However, the presence of water in the microporosity alone is not sufficient to explain this phenomenon. Other factors such as tortuosity/roughness at the probed length scale and/or the presence of channels with restricted water access leading to incomplete filling may also contribute to this effect.

This subset of water molecules that are affected by the silica surface may have different dynamics depending on the probed orientation as illustrated in Table 4 and illustrated in Fig. 10. Indeed, it has been shown that the enthalpy and entropy of the interfacial pore water are higher than those of bulk water due to the increase in disorder induced by the low 2D topology [51]. This means that a single hydrogen bond with a hydroxyl surface site of an interfacial water molecule is stronger than a hydrogen bond in bulk. Moreover, we have shown through Monte Carlo simulations [52] that interfacial water presents a strong distortion of the tetrahedral hydrogen bonds network compared to bulk water. Therefore, it appears more difficult for water molecules to move from one hydroxyl surface site to another compared to forming a hydrogen bond with a water molecule not adsorbed at the surface. This may suggest that the density of hydroxyl groups and the ratio of pore surface to water volume (S/V ratio) drive the difference between the perpendicular and parallel diffusion coefficients at this timescale. In other words, the difference between the two diffusion coefficients may rise with the density of hydroxyl groups and the S/V ratio.

4. Conclusions

The anisotropy of water dynamics confined in highly oriented mesoporous silica with a pore diameter of 5.5 nm was studied in parallel and perpendicular directions to the pore axis. For the first time, we found that water diffusion in silica mesopores is faster in the direction

perpendicular to the pore surface than parallel to it at two picosecond timescales, 7 ps and 30 ps.

The use of such model systems presenting highly oriented mesopores opens new perspectives for studying the confinement effect on water transport at various scales allowing access to the perpendicular and longitudinal water dynamics. Thus, it will be possible, based on additional experiments such as dielectric spectroscopy, NMR relaxometry and water diffusion analysis through the membrane, to investigate the water transport from the molecular to the macroscopic scale in a continuous way.

5. Appendices

A. SEM and TEM images

B. Estimation of the filling ratios R of the alumina pores

The filling ratio of the alumina membranes with silica was determined from SEM images of 12.67×10.95 μm^2 areas. The number of filled alumina pores was estimated by first, modifying the color contrast in the obtained SEM images allowing the determination of the number of empty pores as described on the Fig. B.1. Then the ratio between the filled and the totality of the alumina pores was calculated.

C. Calculation of the absolute scattered intensity

The absolute scattered intensity of the small angle X-ray scattering measurements was obtained based on the following relation [33].

$$I^{abs} = (1/(\Phi.Eff.\Delta\Omega))\ (1/z_b)\ ((I_S^m - 8)/T_s)$$

Where I_S^m (cps) is the measured intensity of the sample, Φ represents the incoming X-ray flux, Eff stands for the detector efficiency, $\Delta\Omega$ is the detection solid angle, T_s is the sample

transmission and z_b is the sample thickness. The term $\Phi.Eff.\Delta\Omega$ is determined by measuring a calibration sample (polyethylene), which has a well-known absolute intensity (4.9 cm^{-1}).

The sample thickness, z_b, was determined from the transmission of the sample T_S as follow [53]:

$$z_b = -(\ln T_S/\mu_b)$$

with μ_b representing the linear absorption of the bulk (non-porous) solid material, ideally spread on z_b. For the hybrid alumina membranes:

$$\mu_b = C_1\ \mu_{Al2O3} + C_2\ \mu_{SiO2}$$

with C_1 and C_2 are the volume fractions of the alumina and silica parts crossed by the X-ray beam respectively. μ_{Al2O3} and μ_{SiO2} are the linear absorptions of the bulk alumina and silica respectively. C_1 and C_2 were calculated based on the SEM images treatment presenting earlier, from which we can calculate the volume of the alumina part in the membrane, then, by suggesting that the silica microfiber length is 10 μm in each filled alumina pore, we can estimate the volumetric proportion of silica and alumina for each sample.

D. Experimental and fitted S (Q, ω) at different Q values.

The experimental and fitted S(Q, ω), at different Q values are presented from Fig. D.1 to Fig. D.4.

Acknowledgements

The Fondation de la Maison de la Chimie is gratefully acknowledged for funding the post-doctoral position of Hassan Khoder. This work is based on experiments performed on the IN5 time-of-flight spectrometer of the Institut Laue-Langevin in Grenoble, France. Beamtime

allocation for the project is gratefully acknowledged. The authors would like to thank Joseph Lautru for the maintenance of DVS tool.

References

[1] C. Tournassat, C.I. Steefel, Reactive Transport Modeling of Coupled Processes in Nanoporous Media, Rev. Mineral. Geochem. 85 (2019) 75–109. https://doi.org/10.2138/rmg.2019.85.4.

[2] P. Jollivet, S. Gin, S. Schumacher, Forward dissolution rate of silicate glasses of nuclear interest in clay-equilibrated groundwater, Chem. Geol. 330–331 (2012) 207–217. https://doi.org/10.1016/j.chemgeo.2012.09.012.

[3] B. Gouze, J. Cambedouzou, S. Parrès-Maynadié, D. Rébiscoul, How hexagonal mesoporous silica evolves in water on short and long term: Role of pore size and silica wall porosity, Microporous Mesoporous Mater. 183 (2014) 168–176. https://doi.org/10.1016/j.micromeso.2013.08.041.

[4] M. Baum, F. Rieutord, D. Rébiscoul, Underlying Processes Driving the Evolution of Nanoporous Silica in Water and Electrolyte Solutions, J. Phys. Chem. C. 124 (2020) 14531–14540. https://doi.org/10.1021/acs.jpcc.0c00911.

[5] A.G. Stack, A. Fernandez-Martinez, L.F. Allard, J.L. Bañuelos, G. Rother, L.M. Anovitz, D.R. Cole, G.A. Waychunas, Pore-Size-Dependent Calcium Carbonate Precipitation Controlled by Surface Chemistry, Environ. Sci. Technol. 48 (2014) 6177–6183. https://doi.org/10.1021/es405574a.

[6] Godinho, Ma, Chai, Storm, Burnett, Mineral Precipitation in Fractures and Nanopores within Shale Imaged Using Time-Lapse X-ray Tomography, Minerals. 9 (2019) 480. https://doi.org/10.3390/min9080480.

[7] S. Gin, C. Guittonneau, N. Godon, D. Neff, D. Rebiscoul, M. Cabié, S. Mostefaoui, Nuclear Glass Durability: New Insight into Alteration Layer Properties, J. Phys. Chem. C. 115 (2011) 18696–18706. https://doi.org/10.1021/jp205477q.

[8] H. Aréna, D. Rébiscoul, E. Garcès, N. Godon, Comparative effect of alkaline elements and calcium on alteration of International Simple Glass, Npj Mater. Degrad. 3 (2019) 10. https://doi.org/10.1038/s41529-019-0072-7.

[9] A. Michelin, E. Burger, D. Rebiscoul, D. Neff, F. Bruguier, E. Drouet, P. Dillmann, S. Gin, Silicate Glass Alteration Enhanced by Iron: Origin and Long-Term Implications, Environ. Sci. Technol. 47 (2013) 750–756. https://doi.org/10.1021/es304057y.

[10] A.B. Grommet, M. Feller, R. Klajn, Chemical reactivity under nanoconfinement, Nat. Nanotechnol. 15 (2020) 256–271. https://doi.org/10.1038/s41565-020-0652-2.

[11] D. Rébiscoul, J. Cambedouzou, I. Matar Briman, M. Cabié, H.-P. Brau, O. Diat, Water Dynamics in Nanoporous Alteration Layer Coming from Glass Alteration: An Experimental Approach, J. Phys. Chem. C. 119 (2015) 15982–15993. https://doi.org/10.1021/acs.jpcc.5b03073.

[12] C.T. Kresge, M.E. Leonowicz, W.J. Roth, J.C. Vartuli, J.S. Beck, Ordered mesoporous molecular sieves synthesized by a liquid-crystal template mechanism, Nature. 359 (1992) 710–712. https://doi.org/10.1038/359710a0.

[13] D. Zhao, J. Feng, Q. Huo, N. Melosh, G.H. Fredrickson, B.F. Chmelka, G.D. Stucky, Triblock Copolymer Syntheses of Mesoporous Silica with Periodic 50 to 300 Angstrom Pores, Science. 279 (1998) 548–552. https://doi.org/10.1126/science.279.5350.548.

[14] A. Rjiba, H. Khoder, J. Jelassi, S. Bouguet-Bonnet, C. Gardiennet, E.-E. Bendeif, A. Gansmüller, R. Dorbez-Sridi, Differential scanning calorimetry and NMR study of water confined in a mesoporous bioactive glass, Microporous Mesoporous Mater. 316 (2021) 110922. https://doi.org/10.1016/j.micromeso.2021.110922.

[15] E. Steiner, S. Bouguet-Bonnet, J.-L. Blin, D. Canet, Water Behavior in Mesoporous Materials As Studied by NMR Relaxometry, J. Phys. Chem. A. 115 (2011) 9941–9946. https://doi.org/10.1021/jp205456g.
[16] S. Takahara, N. Sumiyama, S. Kittaka, T. Yamaguchi, M.-C. Bellissent-Funel, Neutron Scattering Study on Dynamics of Water Molecules in MCM-41. 2. Determination of Translational Diffusion Coefficient, J. Phys. Chem. B. 109 (2005) 11231–11239. https://doi.org/10.1021/jp046036l.
[17] C. Alba-Simionesco, B. Coasne, G. Dosseh, G. Dudziak, K.E. Gubbins, R. Radhakrishnan, M. Sliwinska-Bartkowiak, Effects of confinement on freezing and melting, J. Phys. Condens. Matter. 18 (2006) R15–R68. https://doi.org/10.1088/0953-8984/18/6/R01.
[18] I.M. Briman, D. Rébiscoul, O. Diat, J.-M. Zanotti, P. Jollivet, P. Barboux, S. Gin, Impact of Pore Size and Pore Surface Composition on the Dynamics of Confined Water in Highly Ordered Porous Silica, J. Phys. Chem. C. 116 (2012) 7021–7028. https://doi.org/10.1021/jp3001898.
[19] M. Baum, F. Rieutord, F. Juranyi, C. Rey, D. Rébiscoul, Dynamical and Structural Properties of Water in Silica Nanoconfinement: Impact of Pore Size, Ion Nature, and Electrolyte Concentration, Langmuir. 35 (2019) 10780–10794. https://doi.org/10.1021/acs.langmuir.9b01434.
[20] F.G. Alabarse, J. Haines, O. Cambon, C. Levelut, D. Bourgogne, A. Haidoux, D. Granier, B. Coasne, Freezing of Water Confined at the Nanoscale, Phys. Rev. Lett. 109 (2012) 035701. https://doi.org/10.1103/PhysRevLett.109.035701.
[21] A. Jani, M. Busch, J.B. Mietner, J. Ollivier, M. Appel, B. Frick, J.-M. Zanotti, A. Ghoufi, P. Huber, M. Fröba, D. Morineau, Dynamics of water confined in mesopores with variable surface interaction, J. Chem. Phys. 154 (2021) 094505. https://doi.org/10.1063/5.0040705.
[22] A. Yamaguchi, F. Uejo, T. Yoda, T. Uchida, Y. Tanamura, T. Yamashita, N. Teramae, Self-assembly of a silica–surfactant nanocomposite in a porous alumina membrane, Nat. Mater. 3 (2004) 337–341. https://doi.org/10.1038/nmat1107.
[23] Z. Gong, G. Ji, M. Zheng, X. Chang, W. Dai, L. Pan, Y. Shi, Y. Zheng, Structural Characterization of Mesoporous Silica Nanofibers Synthesized Within Porous Alumina Membranes, Nanoscale Res. Lett. 4 (2009) 1257. https://doi.org/10.1007/s11671-009-9389-4.
[24] Z. Yang, Z. Niu, X. Cao, Z. Yang, Y. Lu, Z. Hu, C.C. Han, Template Synthesis of Uniform 1D Mesostructured Silica Materials and Their Arrays in Anodic Alumina Membranes, Angew. Chem. Int. Ed. 42 (2003) 4201–4203. https://doi.org/10.1002/anie.200250808.
[25] S. Meoto, M.-O. Coppens, Anodic alumina-templated synthesis of mesostructured silica membranes – current status and challenges, J Mater Chem A. 2 (2014) 5640–5654. https://doi.org/10.1039/C3TA15330D.
[26] S. Meoto, N. Kent, M.M. Nigra, M.-O. Coppens, Mesostructure of Mesoporous Silica/Anodic Alumina Hierarchical Membranes Tuned with Ethanol, Langmuir. 33 (2017) 4823–4832. https://doi.org/10.1021/acs.langmuir.7b00453.
[27] A. Yamaguchi, H. Kaneda, W. Fu, N. Teramae, Structural Control of Surfactant-Templated Mesoporous Silica Formed Inside Columnar Alumina Pores, Adv. Mater. 20 (2008) 1034–1037. https://doi.org/10.1002/adma.200701368.
[28] A. Šaki, W. Wien, S. Milosavljevi, Solid-State Backscattered-Electron Detector for Sub-keV Imaging in Scanning Electron Microscopy, (2011) 4.

[29] J. Ollivier, H. Mutka, IN5 Cold Neutron Time-of-Flight Spectrometer, Prepared to Tackle Single Crystal Spectroscopy, J. Phys. Soc. Jpn. 80 (2011) SB003. https://doi.org/10.1143/JPSJS.80SB.SB003.
[30] REBISCOUL Diane, KHODER Hassan, OLLIVIER Jacques, Study of the uniaxial water dynamics in electrolyte solutions confined in oriented silica nanochannels, (n.d.). https://doi.org/10.5291/ILL-DATA.6-07-83.
[31] J.-M. Zanotti, QENSH, (n.d.). https://iramis.cea.fr/Pisp/jean-marc.zanotti/.
[32] C.A. Schneider, W.S. Rasband, K.W. Eliceiri, NIH Image to ImageJ: 25 years of image analysis, Nat. Methods. 9 (2012) 671–675. https://doi.org/10.1038/nmeth.2089.
[33] J. Cambedouzou, O. Diat, Quantitative small-angle scattering on mesoporous silica powders: from morphological features to specific surface estimation, J. Appl. Crystallogr. 45 (2012) 662–673. https://doi.org/10.1107/S0021889812020298.
[34] F. Hoffmann, M. Cornelius, J. Morell, M. Fröba, Silica-Based Mesoporous Organic–Inorganic Hybrid Materials, Angew. Chem. Int. Ed. 45 (2006) 3216–3251. https://doi.org/10.1002/anie.200503075.
[35] A. Heydari-Gorji, Y. Yang, A. Sayari, Effect of the Pore Length on CO_2 Adsorption over Amine-Modified Mesoporous Silicas, Energy Fuels. 25 (2011) 4206–4210. https://doi.org/10.1021/ef200765f.
[36] P. Burguete, A. Beltrán, C. Guillem, J. Latorre, F. Pérez-Pla, D. Beltrán, P. Amorós, Pore Length Effect on Drug Uptake and Delivery by Mesoporous Silicas, ChemPlusChem. 77 (2012) 817–831. https://doi.org/10.1002/cplu.201200099.
[37] Y. Lu, R. Ganguli, C.A. Drewien, M.T. Anderson, C.J. Brinker, W. Gong, Y. Guo, H. Soyez, B. Dunn, M.H. Huang, J.I. Zink, Continuous formation of supported cubic and hexagonal mesoporous films by sol–gel dip-coating, Nature. 389 (1997) 364–368. https://doi.org/10.1038/38699.
[38] C.J. Brinker, Y. Lu, A. Sellinger, H. Fan, Evaporation-Induced Self-Assembly: Nanostructures Made Easy, Adv. Mater. 11 (1999) 579–585. https://doi.org/10.1002/(SICI)1521-4095(199905)11:7<579::AID-ADMA579>3.0.CO;2-R.
[39] J. Teixeira, M.C. Bellissent-Funel, S.H. Chen, A.J. Dianoux, Experimental determination of the nature of diffusive motions of water molecules at low temperatures, Phys. Rev. A. 31 (1985) 1913–1917. https://doi.org/10.1103/PhysRevA.31.1913.
[40] A.J. Dianoux, F. Volino, H. Hervet, Incoherent scattering law for neutron quasi-elastic scattering in liquid crystals, Mol. Phys. 30 (1975) 1181–1194. https://doi.org/10.1080/00268977500102721.
[41] N. Malikova, S. Longeville, J.-M. Zanotti, E. Dubois, V. Marry, P. Turq, J. Ollivier, Signature of Low-Dimensional Diffusion in Complex Systems, Phys. Rev. Lett. 101 (2008) 265901. https://doi.org/10.1103/PhysRevLett.101.265901.
[42] L. Van Hove, Correlations in Space and Time and Born Approximation Scattering in Systems of Interacting Particles, Phys. Rev. 95 (1954) 249–262. https://doi.org/10.1103/PhysRev.95.249.
[43] G.H. Vineyard, Scattering of Slow Neutrons by a Liquid, Phys. Rev. 110 (1958) 999–1010. https://doi.org/10.1103/PhysRev.110.999.
[44] B. Siboulet, J. Molina, B. Coasne, P. Turq, J.-F. Dufreche, Water self-diffusion at the surface of silica glasses: effect of hydrophilic to hydrophobic transition, Mol. Phys. 111 (2013) 3410–3417. https://doi.org/10.1080/00268976.2013.861084.
[45] M. Rovere, P. Gallo, Effects of confinement on static and dynamical properties of water, Eur. Phys. J. E. 12 (2003) 77–81. https://doi.org/10.1140/epje/i2003-10027-5.

[46] P.A. Bonnaud, B. Coasne, R.J.-M. Pellenq, Molecular simulation of water confined in nanoporous silica, J. Phys. Condens. Matter. 22 (2010) 284110. https://doi.org/10.1088/0953-8984/22/28/284110.
[47] J. Qvist, H. Schober, B. Halle, Structural dynamics of supercooled water from quasielastic neutron scattering and molecular simulations, J. Chem. Phys. 134 (2011) 144508. https://doi.org/10.1063/1.3578472.
[48] N.C. Osti, A. Coté, E. Mamontov, A. Ramirez-Cuesta, D.J. Wesolowski, S.O. Diallo, Characteristic features of water dynamics in restricted geometries investigated with quasi-elastic neutron scattering, Chem. Phys. 465–466 (2016) 1–8. https://doi.org/10.1016/j.chemphys.2015.11.008.
[49] Y. Marcus, Ions in Solution and their Solvation: Marcus/Ions in Solution and their Solvation, John Wiley & Sons, Inc, Hoboken, NJ, 2015. https://doi.org/10.1002/9781118892336.
[50] J. Teixeira, J.-M. Zanotti, M.-C. Bellissent-Funel, S.-H. Chen, Water in confined geometries, Phys. B Condens. Matter. 234–236 (1997) 370–374. https://doi.org/10.1016/S0921-4526(96)00991-X.
[51] J.-M. Zanotti, P. Judeinstein, S. Dalla-Bernardina, G. Creff, J.-B. Brubach, P. Roy, M. Bonetti, J. Ollivier, D. Sakellariou, M.-C. Bellissent-Funel, Competing coexisting phases in 2D water, Sci. Rep. 6 (2016) 25938. https://doi.org/10.1038/srep25938.
[52] H. Khoder, D. Schaniel, S. Pillet, E.-E. Bendeif, X-ray scattering study of water confined in bioactive glasses: experimental and simulated pair distribution function, Acta Crystallogr. Sect. Found. Adv. 76 (2020) 589–599. https://doi.org/10.1107/S2053273320007834.
[53] O. Spalla, S. Lyonnard, F. Testard, Analysis of the small-angle intensity scattered by a porous and granular medium, J. Appl. Crystallogr. 36 (2003) 338–347. https://doi.org/10.1107/S0021889803002279.

Tables

Table 1. Sample references corresponding to the ethanol mass and aspiration pressures used in preparing the sols and hybrid alumina pores, respectively.

Reference of the sample	Mass of ethanol (g)	Aspiration pressure (kPa)
4Et_20	4	20
4Et_50		50
8Et_20	8	20
8Et_40		40
15Et_20	15	20
15Et_30		30
20Et_20	20	20
20Et_15		15
25Et_20	25	20
25Et_10		10

Table 2. Filling ratios, R, of the hybrid alumina membranes and silica mass density per volume of alumina, d_{SiO2}.

Sample	R	Silica mass density (g_{SiO_2} /$cm^3_{Al_2O_3}$)
4Et_20	0.65	0.078
4Et_50	0.90	0.108
8Et_20	0.20	0.024
8Et_40	0.75	0.090
15Et_20	0.85	0.102
15Et_30	0.60	0.072
20Et_15	0.45	0.054
20Et_20	0.30	0.036
25Et_10	0.30	0.036
25Et_20	0.10	0.012

Table 3. Textural parameters obtained by SAXS and DVS for samples presenting Bragg peaks, the scattering vector q_{10} corresponding to the B1 (10) peak, the interreticular distance d_{10}, the unit cell parameter a, the specific surface area S_{BET}, the porous volume V_p, the mean pore diameter D_p, and the wall thickness.

Sample	q_{10} (nm^{-1})	d_{10} (nm)	a (nm)	S_{BET} (m^2/g_{SiO_2})	V_p (cm^3/g_{SiO_2})	D_p (nm)	wall thickness (nm)
4Et_50	0.74	8.5	9.8	135.5	0.72	5.5	4.3
8Et_40	0.76	8.2	9.4	132.3	0.62	5.5	3.9
15Et_20	0.8	7.9	9.1	101.0	0.36	5.5	3.6
20Et_15	0.85	7.6	8.7	61.6	0.097	-	-

Table 4. Diffusion coefficients obtained from the anisotropic model using λ = 4.8 and 8 Å.

	D_T ($\times 10^{-9}$ m^2 s^{-1})		Para/Perp
	Para	Perp	
λ = 4.8 Å	1.30 ± 0.15	1.90 ± 0.20	0.68 ± 0.15
λ = 8 Å	0.35 ± 0.03	0.61 ± 0.05	0.57 ± 0.10

Figure captions

Fig. 1. Illustrations of (a) the experimental setup used in the preparation of the hybrid alumina membrane and (b) filled alumina pore before and after the thermal treatment at 500 °C [25].

Fig. 2. SEM images of the surface of the hybrid alumina membranes used to calculate the filling ratio R.

Fig. 3. (a) SAXS patterns of the hybrid alumina membranes, (b) evolution of the intensity of the peak B1 (10) after baseline subtraction as a function of the mass density of silica in the membranes d_{SiO2}, and (c) scheme presenting the unit cell parameter a and the interreticular distance d defining the hexagonal arrangement of the mesopores.

Fig. 4. Domains of aspiration pressure vs. ethanol loading corresponding to the filling of alumina pores by the silica. Red regions show the domains having 1D mesopores orientation, and black regions show the 3D and 1D:3D mixture mesopores orientations. TEM images of the silica microfibers in each region are also presented.

Fig. 5. (a) Water adsorption-desorption isotherms, (b) corresponding pore size distributions obtained from the BJH model for the various samples, and (c) kinetics of water vapor adsorption at RH = 95% through the samples 4Et_50 and 15Et_20 having 3D and 1D mesopores orientations respectively.

Fig. 6. (a) Sketch showing the sample orientations with respect to the scattering vector $\vec{Q}$, $\overrightarrow{k_i} = \overrightarrow{k_f} + \vec{Q}$. $\overrightarrow{k_i}$ and $\overrightarrow{k_f}$ are the incident and the scattered wave vectors, respectively. $\overrightarrow{Q_{\parallel}}$ and $\overrightarrow{Q_{\perp}}$ denote the parallel and perpendicular scattering vectors, respectively. θ is the scattering angle. (b) Sketch of a silica mesopore showing the parallel and perpendicular diffusion coefficients.

Fig. 7. QENS spectra of the hydrated samples collected at parallel (45°) and perpendicular (135°) orientations corresponding to (a) Q = 1.85 $Å^{-1}$ for λ = 4.8 Å and (b) Q=1.11 $Å^{-1}$ for λ = 8 Å. Spectra of the dried sample and the vanadium are also shown at the same Q values.

Fig. 8. Fitted curves at the (a) parallel and (b) perpendicular Q values using the model described in eq 1. The parameters obtained from the fitting of the parallel spectra were used and fixed to fit the perpendicular one.

Fig. 9. Fitted curves of the QENS spectra at the parallel and perpendicular Q values using the model described in eq 4. (a) parallel and (b) perpendicular orientations corresponding to Q = 1.85 $Å^{-1}$ for λ = 4.8 Å, (c) parallel and (d) perpendicular orientations corresponding to Q = 1.11 $Å^{-1}$ for λ = 8 Å.

Fig. 10. (a) Scheme of a silica mesopore filled with water (interfacial and bulk) showing the parallel and the perpendicular diffusion coefficients and (b) water molecules interacting with hydroxyl groups at the pore surface with their possible diffusion.

Fig. A.1 SEM images of (a) the front side and (b) the backside of the alumina membrane surface. It shows a non-uniform pore diameter varying from 30 nm on the front side to 200 nm on the backside.

Fig. A.2 TEM images of silica microfibers, after complete etching of the alumina part, showing that the average length of the silica microfibers is comprised between 8 and 11 μm.

Fig. A.3 TEM images of the silica microfibers of 15Et_20 showing a one-dimensional pores orientation.

Fig. A.4 TEM image of silica microfiber showing an inter-pore distance of 10.5 nm.

Fig. B.1 (a) SEM image of the surface of a hybrid alumina membrane treated with ImageJ software in (b) and (c) to determine the ratio of the filled alumina pores.

Fig. D.1 Experimental and fitted S (Q, ω) of the parallel orientation measured with λ = 4.8 Å at Q = 0.35, 0.55, 1.35, 1.5, 1.75 and 1.95 $Å^{-1}$.

Fig. D.2 Experimental and fitted S (Q, ω) of the perpendicular orientation measured with λ = 4.8 Å at Q = 0.35, 0.55, 1.35, 1.5, 1.75 and 1.95 $Å^{-1}$.

Fig. D.3 Experimental and fitted S (Q, ω) of the parallel orientation measured with λ = 8 Å at Q = 0.25, 0.85, 1.0, and 1.15 $Å^{-1}$.

Fig. D.4 Experimental and fitted S (Q, ω) of the perpendicular orientation measured with λ = 8 Å at Q = 0.25, 0.85, 1.0, and 1.15 $Å^{-1}$.

Figures

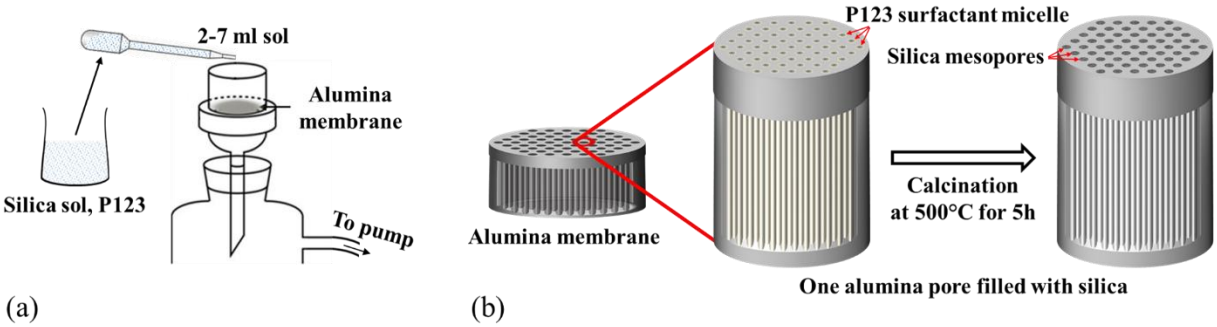

Fig. 1

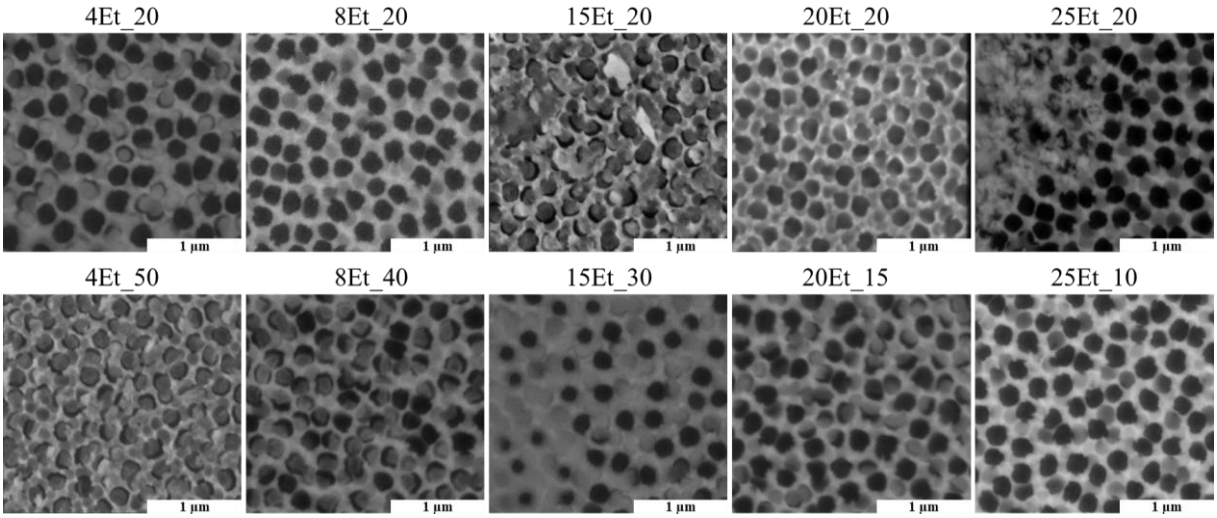

Fig. 2

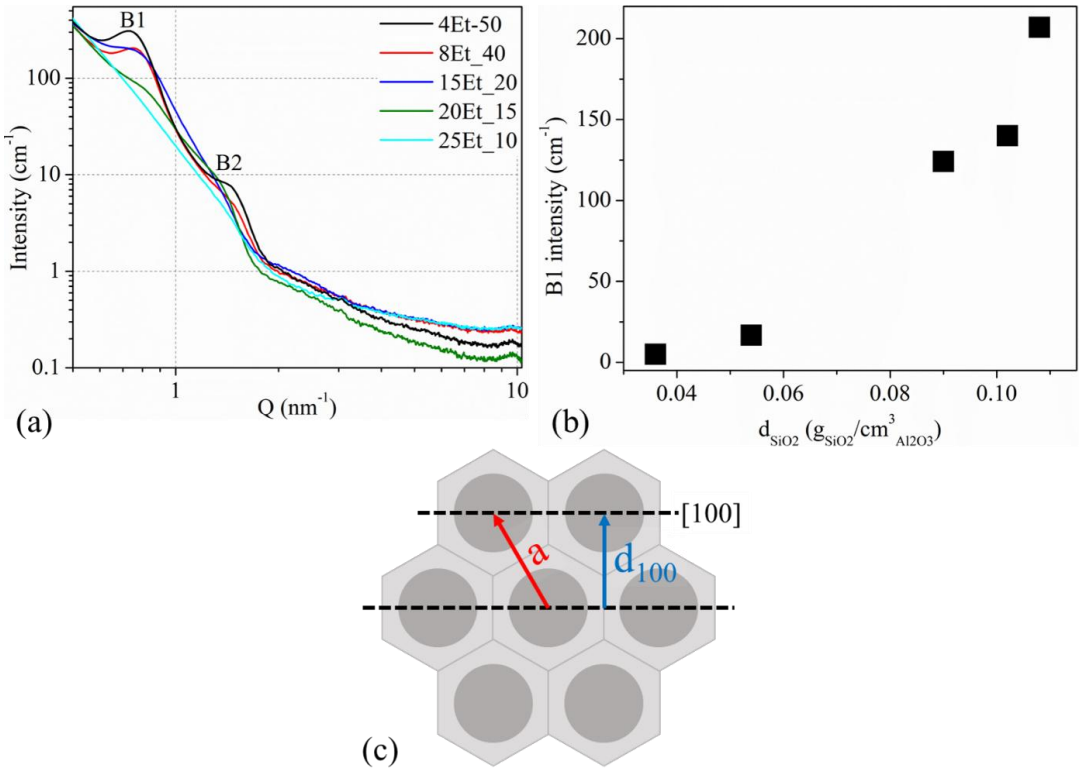
B1
B2
4Et-50
8Et_40
15Et_20
20Et_15
25Et_10
Intensity (cm-1)
Q (nm-1)
(a)
B1 intensity (cm-1)
dSiO2 (gSiO2/cm3Al2O3)
(b)
[100]
a
d100
(c)

Fig. 3

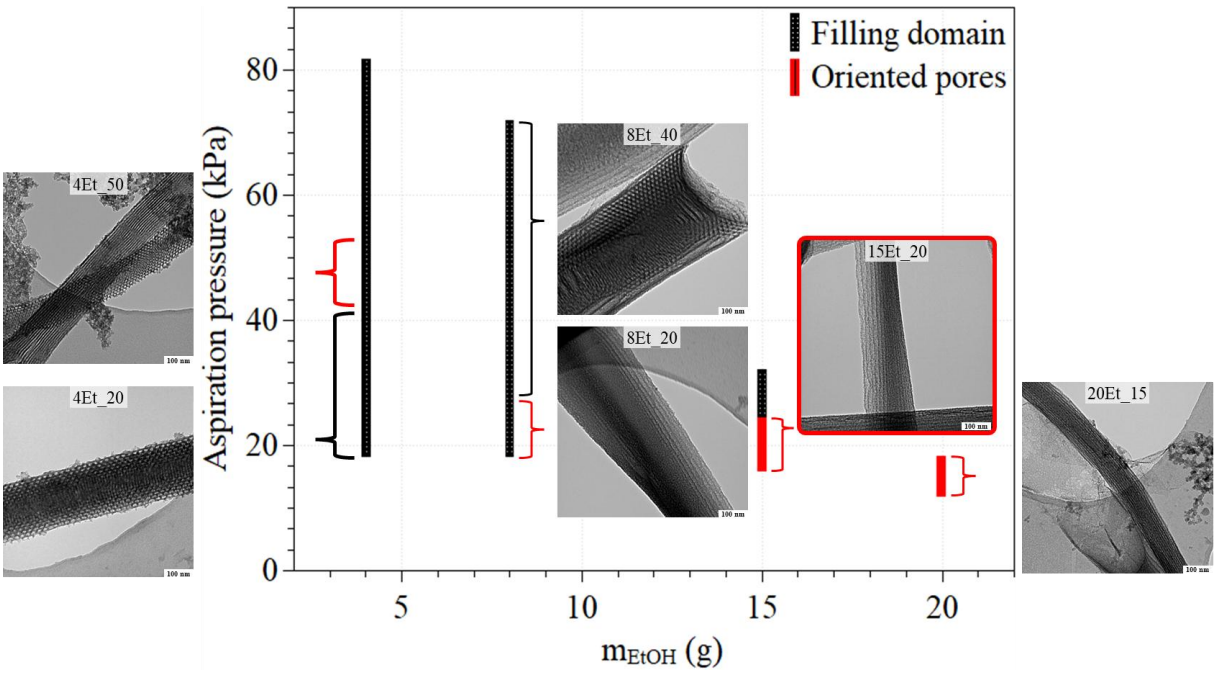
Filling domain
Oriented pores
Aspiration pressure (kPa)
mEtOH (g)
4Et_50
4Et_20
8Et_40
8Et_20
15Et_20
20Et_15

Fig. 4

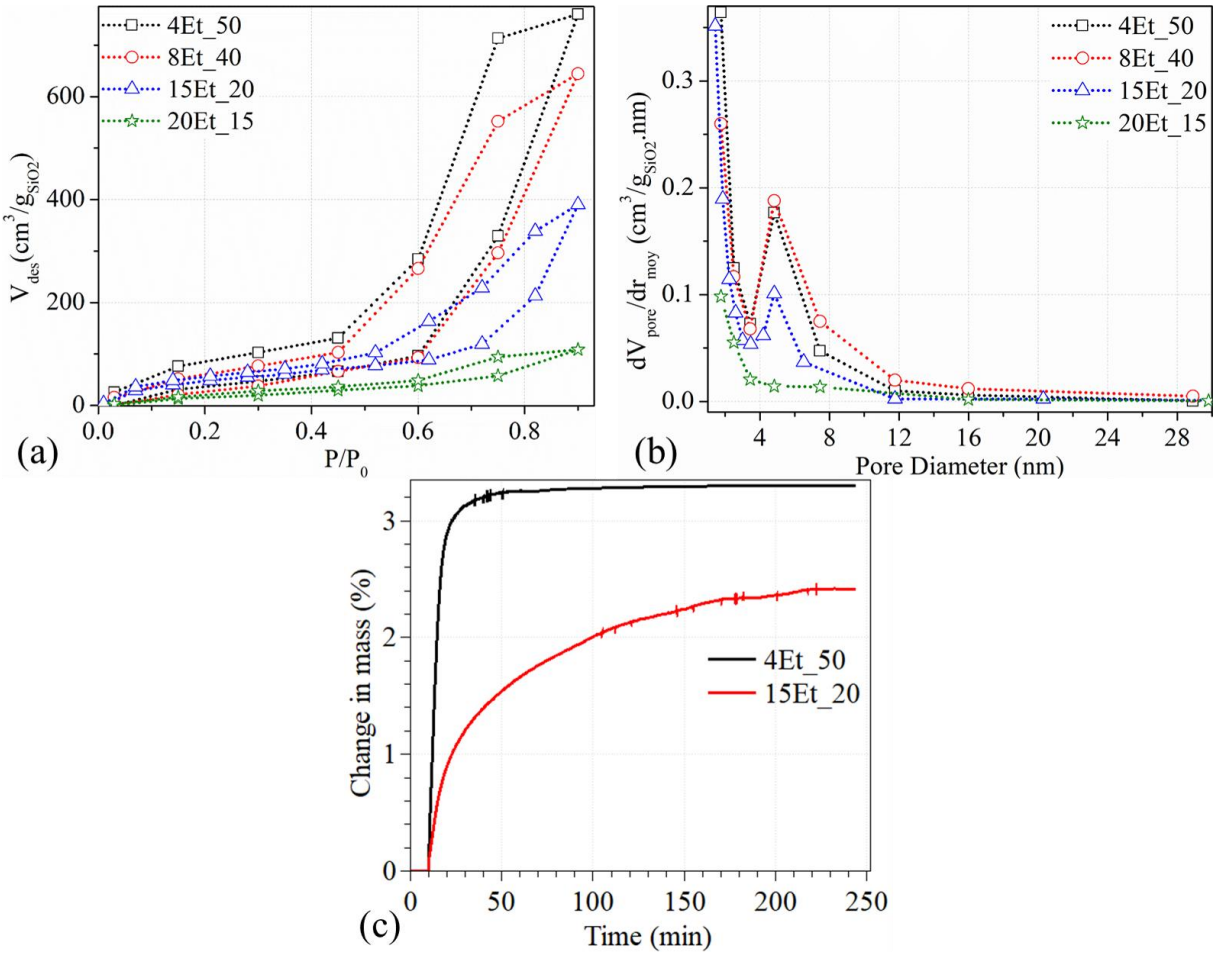
4Et_50
8Et_40
15Et_20
20Et_15
V_{des} (cm^3/g_{SiO2})
P/P$_0$
(a)
dV_{pore}/dr_{moy} (cm^3/g_{SiO2}.nm)
Pore Diameter (nm)
(b)
Change in mass (%)
Time (min)
(c)

Fig. 5

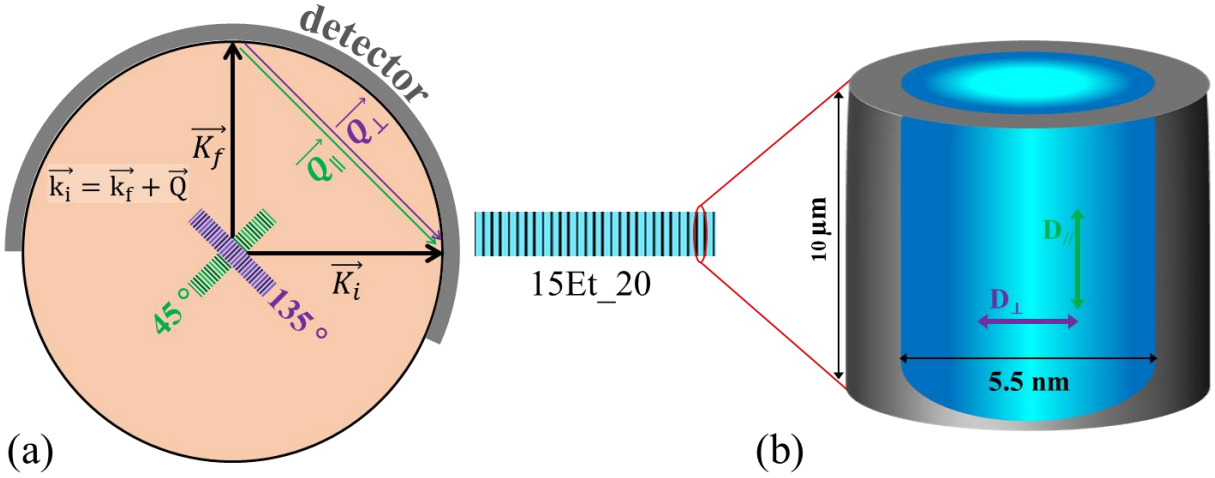
detector
$\vec{K_f}$
$\vec{K_i}$
$\vec{k_i} = \vec{k_f} + \vec{Q}$
$Q^{\perp}$
$Q^{//}$
45°
135°
(a)
15Et_20
10 µm
$D_{//}$
$D_{\perp}$
5.5 nm
(b)

Fig. 6

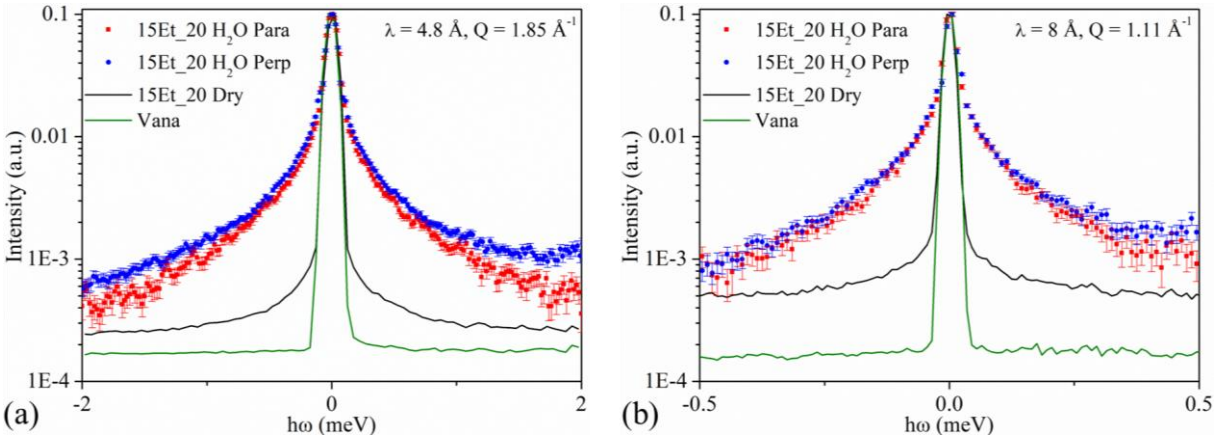
15Et_20 H2O Para
15Et_20 H2O Perp
15Et_20 Dry
Vana
λ = 4.8 Å, Q = 1.85 Å-1
λ = 8 Å, Q = 1.11 Å-1
Intensity (a.u.)
hω (meV)
(a)
(b)

Fig. 7

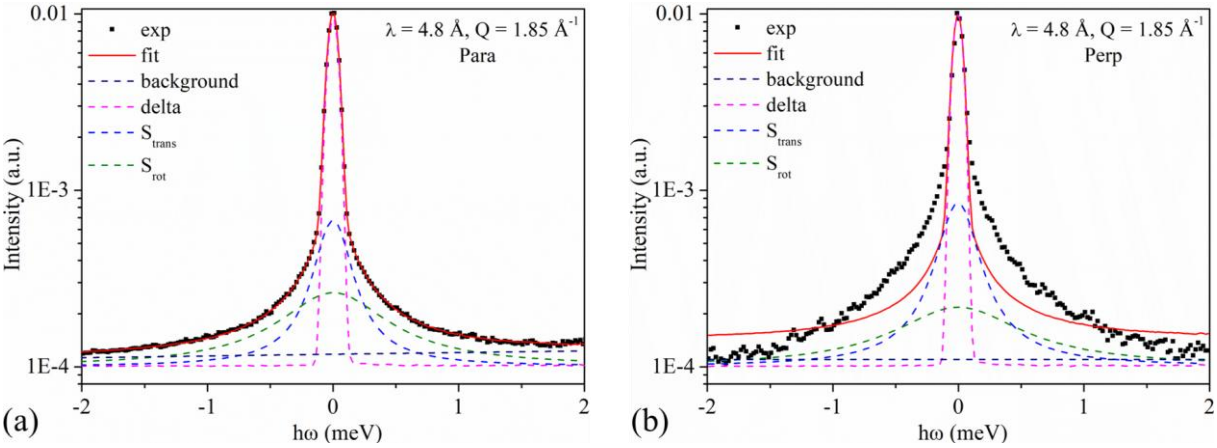
exp
fit
background
delta
Strans
Srot
λ = 4.8 Å, Q = 1.85 Å-1
Para
Perp
Intensity (a.u.)
hω (meV)
(a)
(b)

Fig. 8

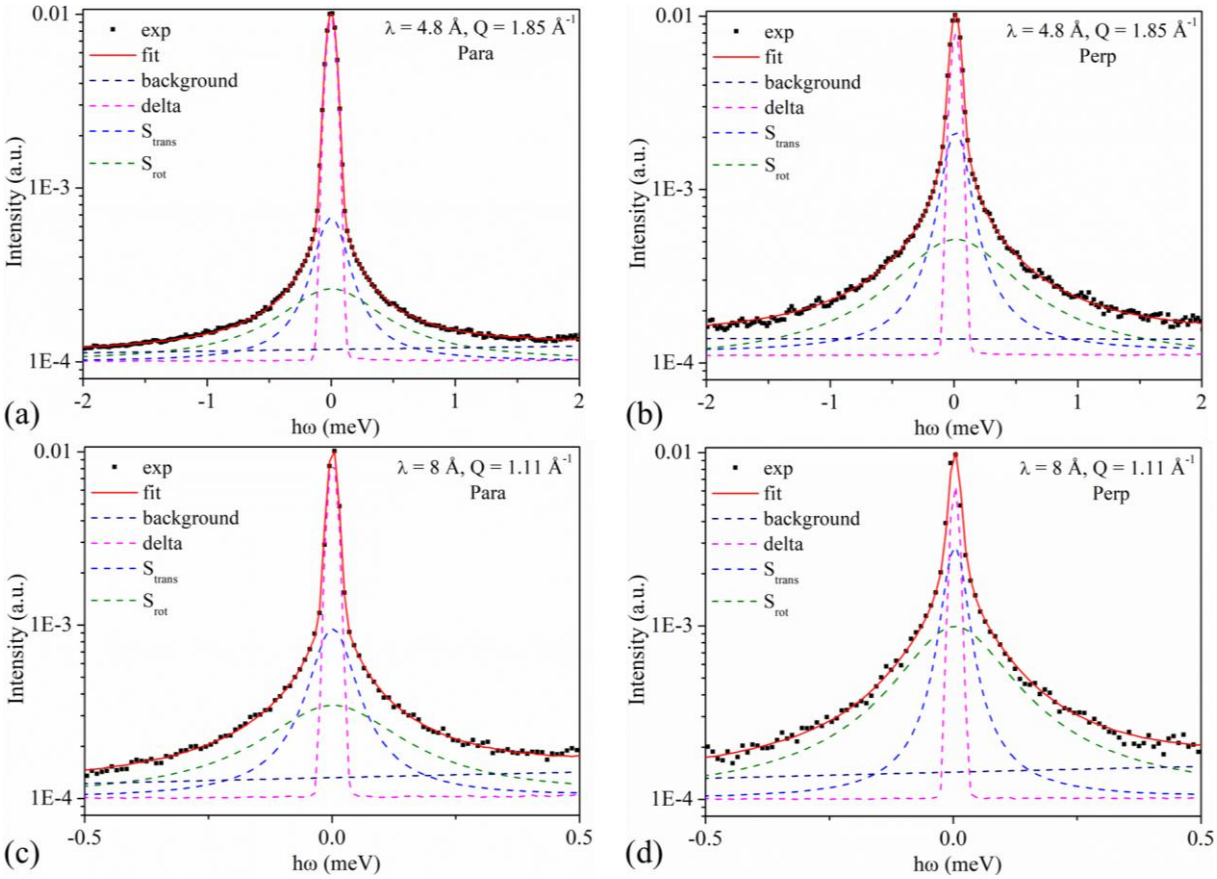
(a)
(b)
(c)
(d)
exp
fit
background
delta
S trans
S rot
λ = 4.8 Å, Q = 1.85 Å-1
Para
Perp
λ = 8 Å, Q = 1.11 Å-1
Intensity (a.u.)
hω (meV)
0.01
1E-3
1E-4

Fig. 9

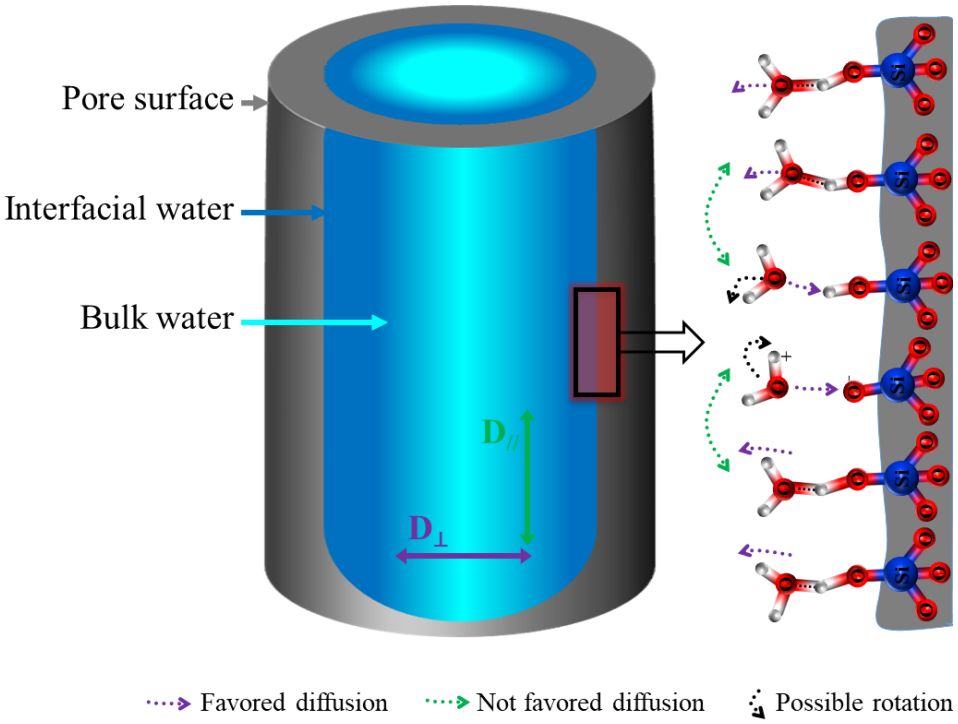
Pore surface
Interfacial water
Bulk water
D//
D⊥
Favored diffusion
Not favored diffusion
Possible rotation

Fig. 10

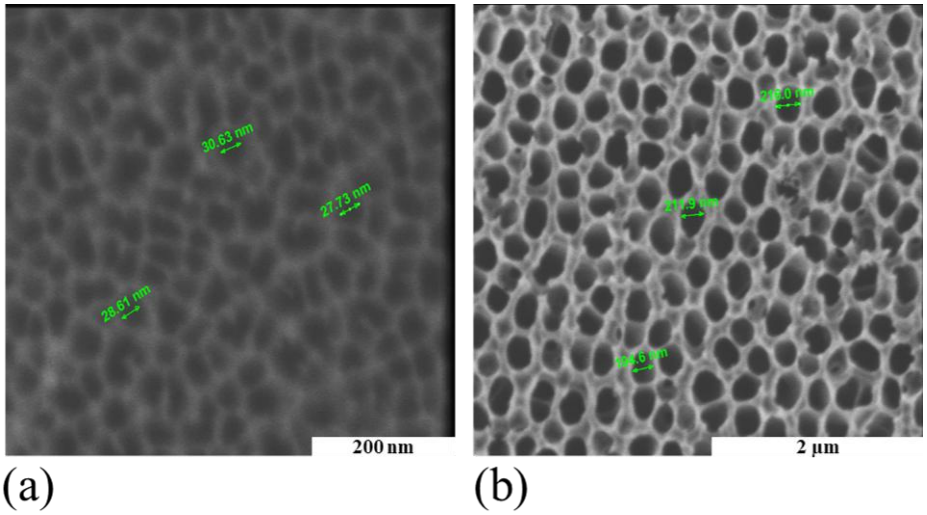

Fig. A.1

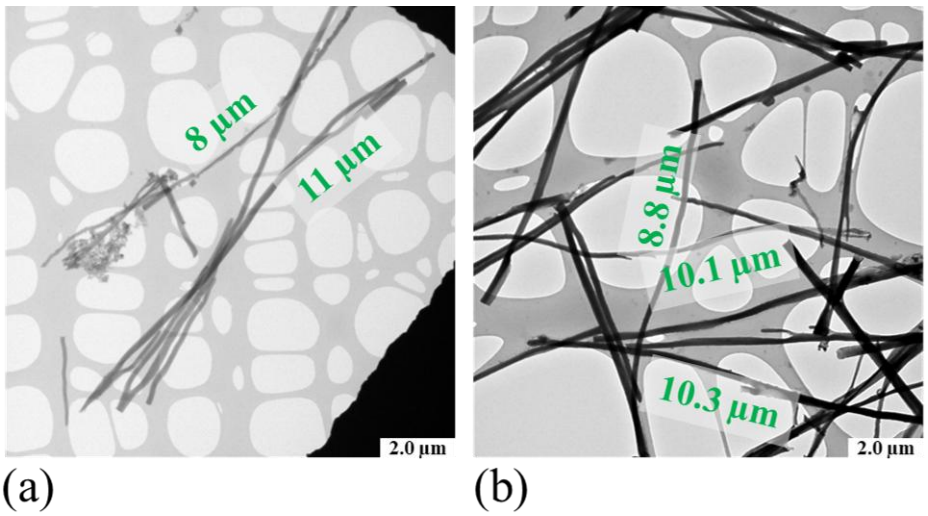

Fig. A.2

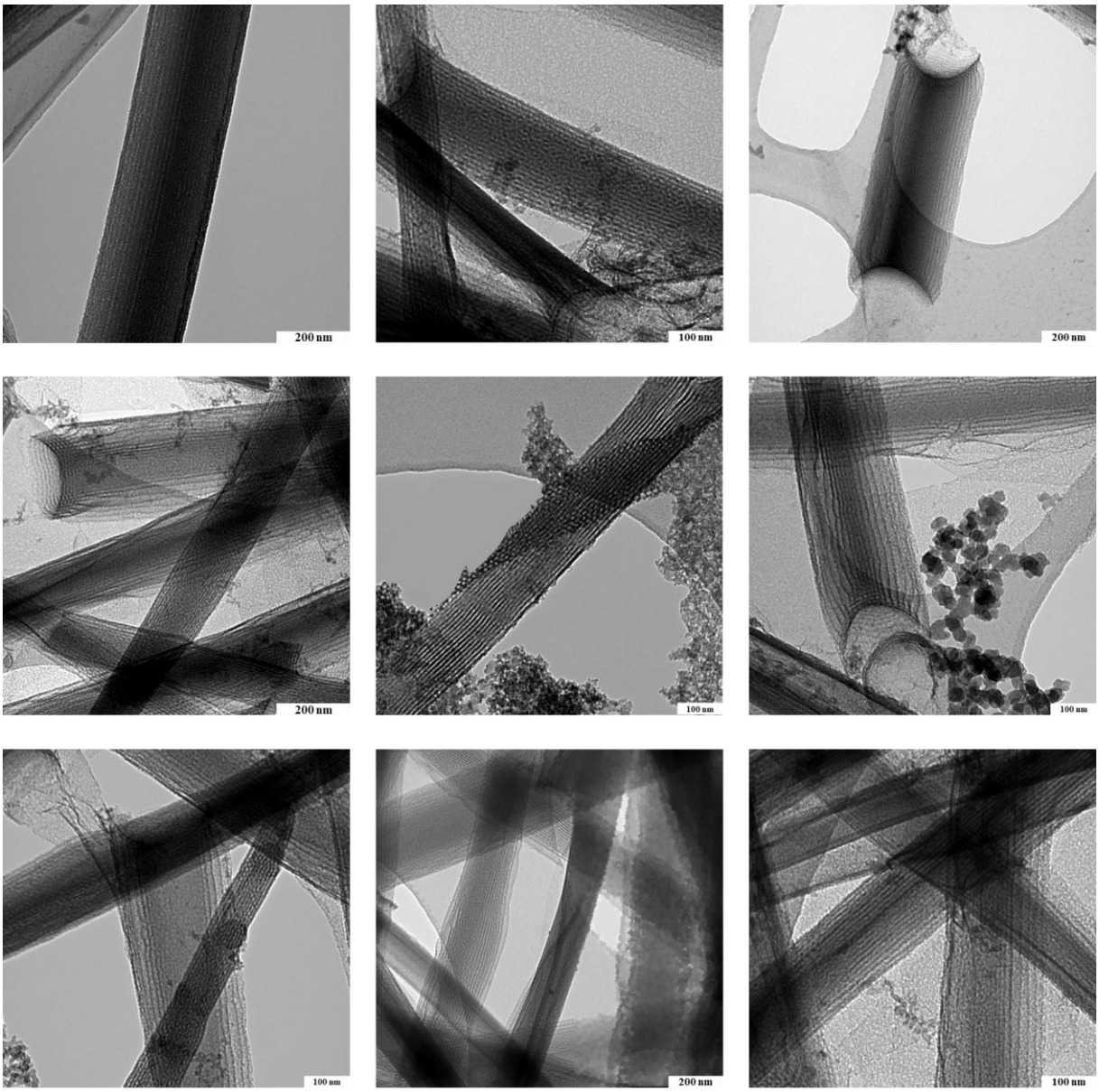

Fig. A.3

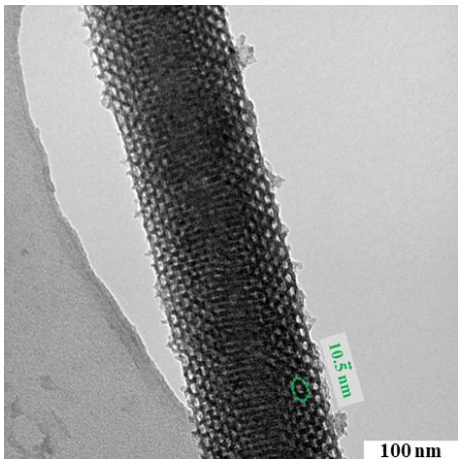

Fig. A.4

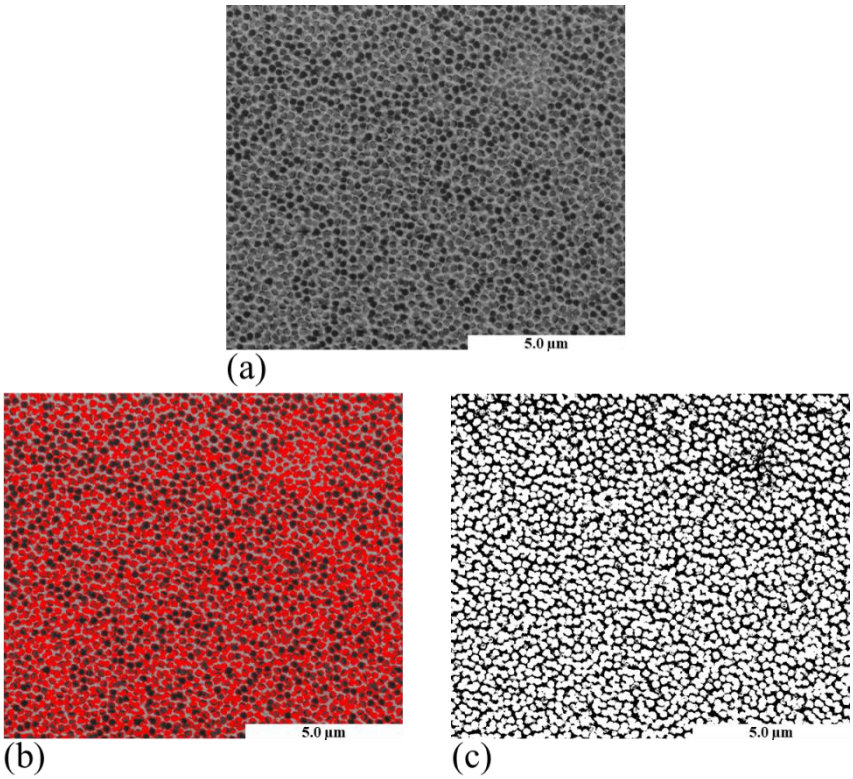

Fig. B.1

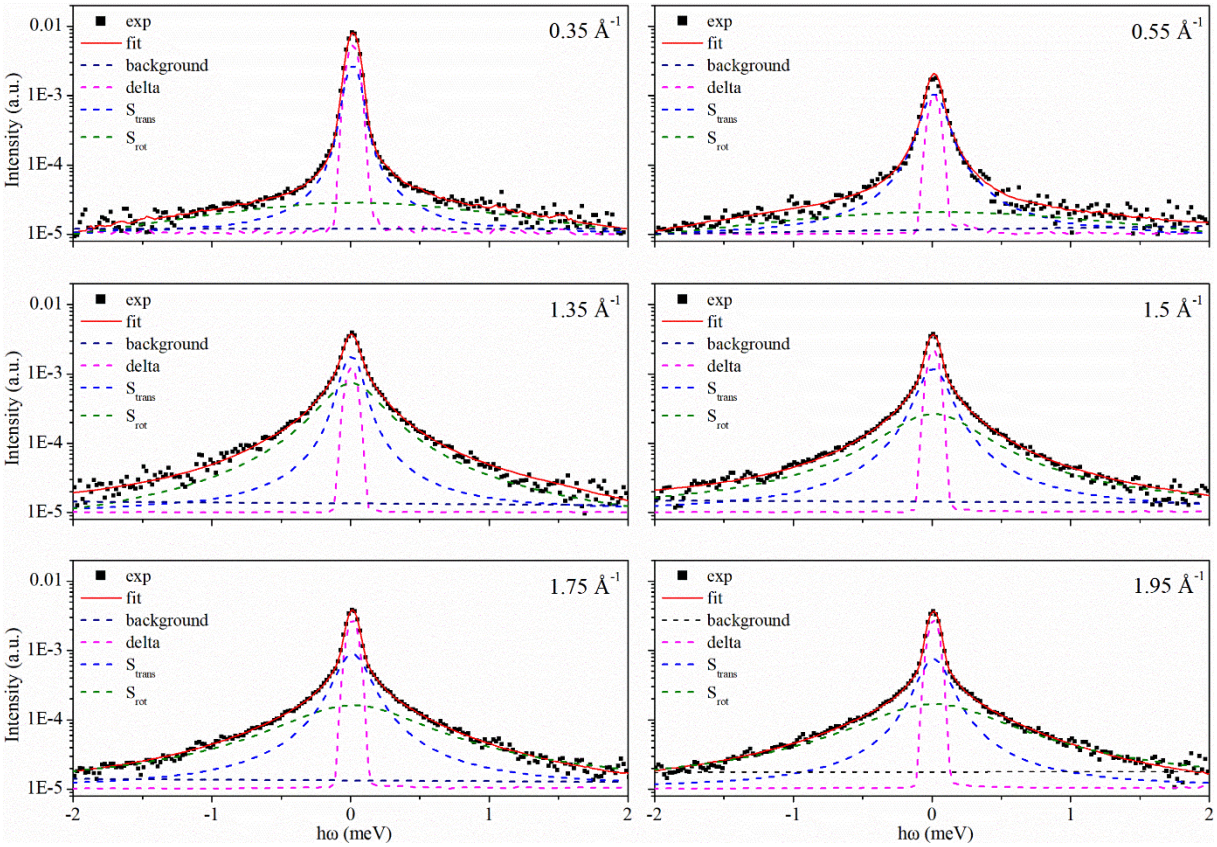
0.35 Å-1
0.55 Å-1
1.35 Å-1
1.5 Å-1
1.75 Å-1
1.95 Å-1
exp
fit
background
delta
Strans
Srot
Intensity (a.u.)
0.01
1E-3
1E-4
1E-5
-2
-1
0
1
2
hω (meV)

Fig. D.1

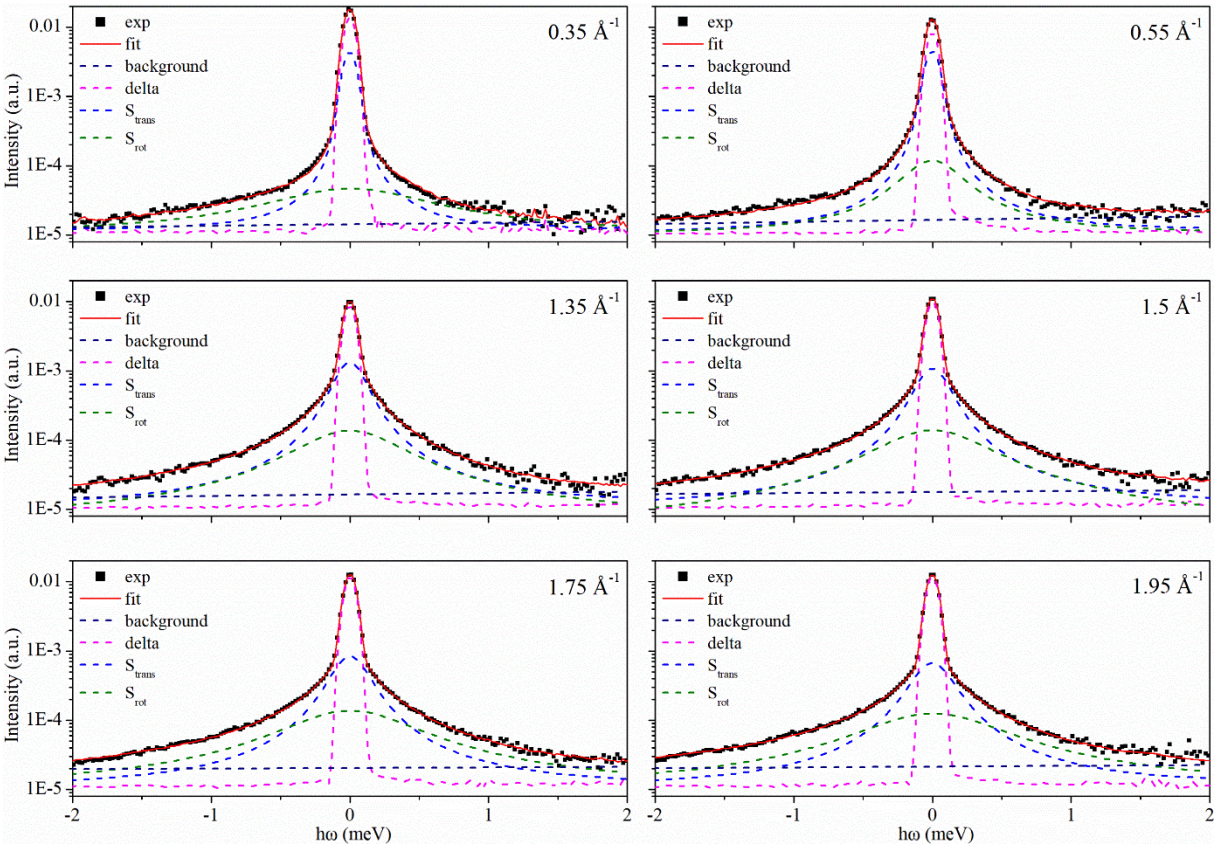
exp
fit
background
delta
S trans
S rot
0.35 Å-1
0.55 Å-1
1.35 Å-1
1.5 Å-1
1.75 Å-1
1.95 Å-1
Intensity (a.u.)
0.01
1E-3
1E-4
1E-5
-2
-1
0
1
2
hω (meV)

Fig. D.2

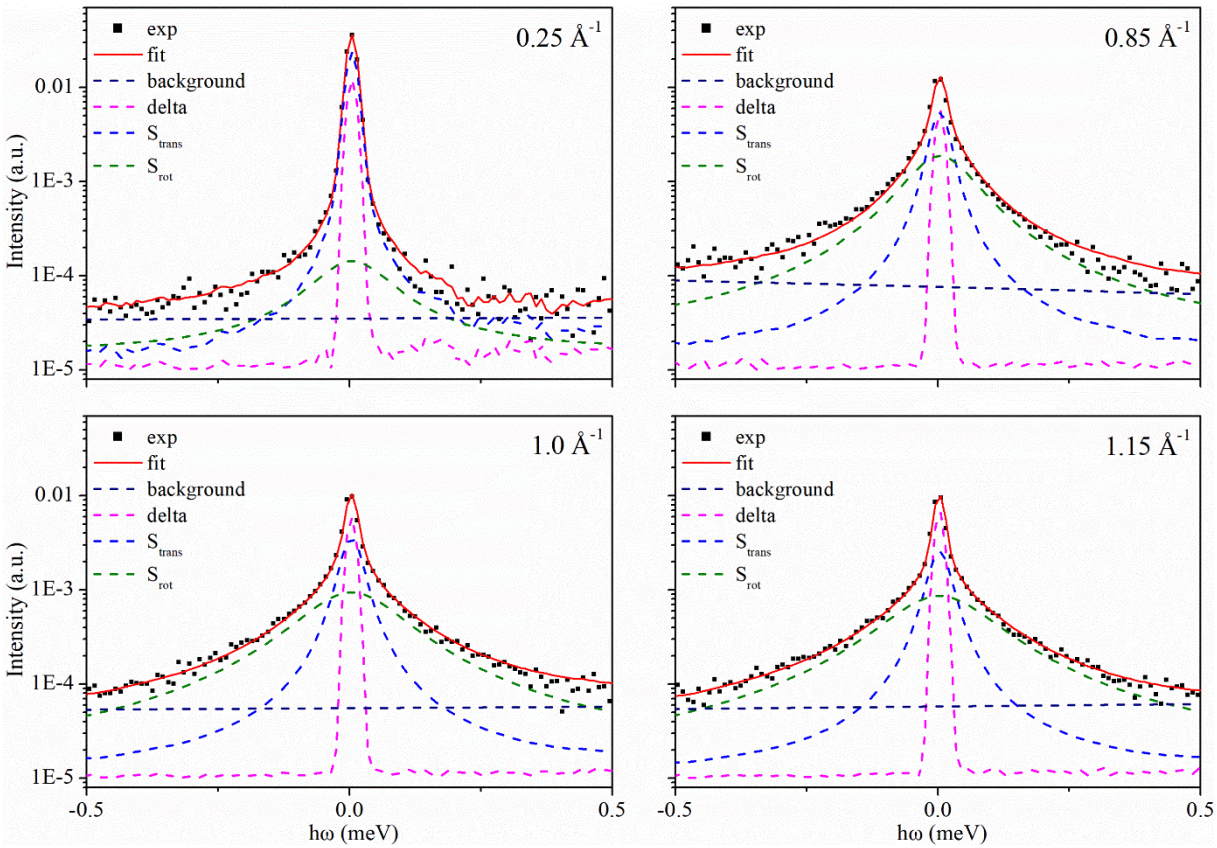
exp
fit
background
delta
S trans
S rot
0.25 Å-1
0.85 Å-1
1.0 Å-1
1.15 Å-1
Intensity (a.u.)
0.01
1E-3
1E-4
1E-5
-0.5
0.0
0.5
hω (meV)

Fig. D.3

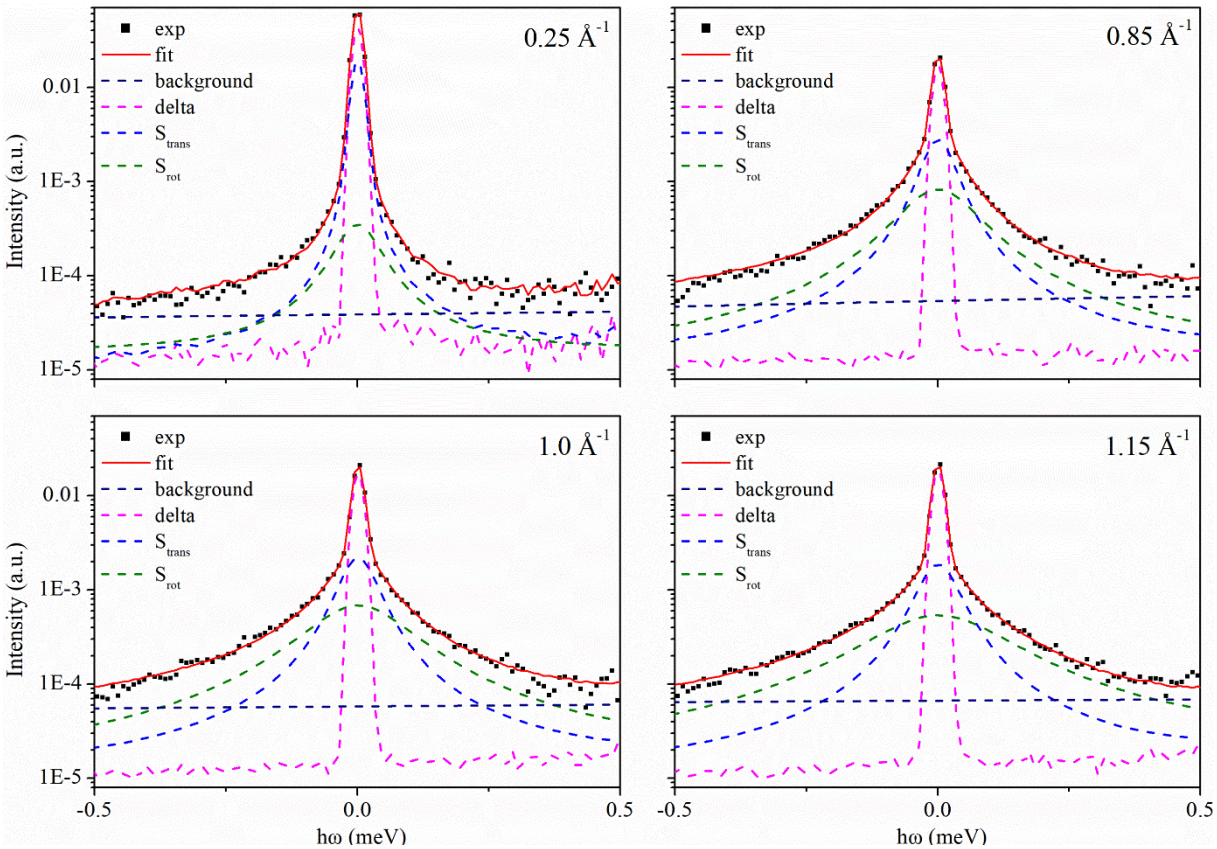
exp
fit
background
delta
S trans
S rot
0.25 Å-1
0.85 Å-1
1.0 Å-1
1.15 Å-1
Intensity (a.u.)
0.01
1E-3
1E-4
1E-5
-0.5
0.0
0.5
hω (meV)

Fig. D.4